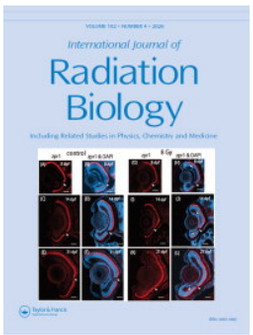

International Journal of Radiation Biology

ISSN: 0955-3002 (Print) 1362-3095 (Online) Journal homepage: www.tandfonline.com/journals/irab20

A metal ion-dependent mechanism promoting gain of function in NEIL1 variants

Jamie T. Zuckerman, Irina G. Minko, Terry P. Lybrand, Martin Egli, Amanda K. McCullough & R. Stephen Lloyd

To cite this article: Jamie T. Zuckerman, Irina G. Minko, Terry P. Lybrand, Martin Egli, Amanda K. McCullough & R. Stephen Lloyd (13 Apr 2026): A metal ion-dependent mechanism promoting gain of function in NEIL1 variants, International Journal of Radiation Biology, DOI: 10.1080/09553002.2026.2654426

To link to this article: https://doi.org/10.1080/09553002.2026.2654426

Published online: 13 Apr 2026.

INTERNATIONAL JOURNAL OF RADIATION BIOLOGY
https://doi.org/10.1080/09553002.2026.2654426

Taylor & Francis
by informa

ORIGINAL ARTICLE

A metal ion-dependent mechanism promoting gain of function in NEIL1 variants

Jamie T. Zuckerman[a], Irina G. Minko[a], Terry P. Lybrand[b], Martin Egli[c], Amanda K. McCullough[a,d] and R. Stephen Lloyd[a,d]

[a]Oregon Institute of Occupational Health Sciences, Oregon Health & Science University, Portland, OR, USA; [b]Department of Chemistry and Center for Structural Biology, Vanderbilt University, Nashville, TN, USA; [c]Department of Biochemistry, School of Medicine, Vanderbilt Ingram Cancer Center, Vanderbilt Center for Structural Biology, Vanderbilt University, Nashville, TN, USA; [d]Department of Molecular and Medical Genetics, Oregon Health & Science University, Portland, OR, USA

ABSTRACT

Purpose: Maintenance of genomic integrity following ionizing radiation (IR) and chemical exposures is primarily a function of the base excision repair (BER) pathway. This genome surveillance is initiated by DNA glycosylases, with the endonuclease VIII-like 1 (NEIL1) glycosylase, apurinic/apyrimidinic site (AP) lyase being responsible for the release of IR-induced DNA lesions. Suppressed expression of *NEIL1* leads to increased IR cytotoxicity. Previous analyses of a single nucleotide polymorphic (SNP) variant of NEIL1, Thr103Ala (T103A), revealed compromised catalytic activities. This investigation was designed to determine the mechanisms underlying the deficiencies of T103A.

Materials and methods: Mutant and variant NEIL1 enzymes were constructed and characterized for their ability to catalyze incision of DNAs containing site-specific base damages. Molecular dynamics (MD) simulations of wild-type (WT) and T103A variant NEIL1 using the NEIL1 crystal structure, addressed mechanisms conferring catalytic activity changes.

Results: The glycosylase and AP lyase activities of NEIL1 T103A could be partially restored in the presence of Mg^{2+}. The catalytic activities of T103S were also stimulated by this metal. Similar increases of the reaction rates of T103A and T103S were observed in the presence of Ca^{2+}. In contrast, the activities of WT NEIL1 and T103V mutant were not stimulated by the addition of these metals. MD simulations reveal that the surface loop (residues 102-110) displays enhanced conformational fluctuations in the T103A variant compared to that region in WT NEIL1. Mg^{2+} hexahydrate coordinated to carbonyl oxygens of loop residues dampens loop dynamics.

Conclusion: This study is the first report of the metal-dependent stimulation of compromised activities in a DNA glycosylase variant. The MD simulations suggest that Mg^{2+} stabilizes the surface loop dynamics in the T103A variant, with the effects of the T to A substitution and Mg^{2+} presence being transmitted over a distance greater than 26 Å to the NEIL1 active site.

ARTICLE HISTORY
Received 10 November 2025
Revised 16 March 2026
Accepted 16 March 2026

KEYWORDS
Base excision repair; single nucleotide polymorphic variants; DNA glycosylase; apurinic/apyrimidinic lyase; mutagenesis

1. Introduction

The formation of cellular damage following ionizing radiation (IR) exposures affects all major cellular components including lipids, proteins, and nucleic acids (Ward 1988; Becker et al. 2010; Becker et al. 2020). The amount and distribution of these damages are known to be highly dependent on the specific properties, quality, and absorbed dose of the radiation energy [(Goodhead 1994; Rezaee and Adhikary 2024); reviewed in Averbeck and Rodriguez-Lafrasse (2021)]. Relative to the size of the target molecule, the deposition of energy is best described by linear-energy transfer and is directly related to the source of irradiation and the environment of the biological samples being radiated. Most of the damage conferred to DNA arises from the ionization of water, with the frequency of base modification occurring several orders of magnitude greater than that for single- or double-stranded breaks. Although double-stranded breaks best correlate with cytotoxicity, base modifications can lead to mutagenesis and transcriptional errors. Additionally, if unrepaired, further enzymatic processing of these sites can lead to the conversion to double-stranded breaks and lethality.

Given both the relative abundance of IR-induced base damage and the adverse biological outcomes from lack of repair, cells have a multi-enzyme pathway, base excision repair (BER), that is dedicated to recognizing, removing, and repairing base lesions and adducts. Due to the extent of potential base modifications, cells utilize various DNA glycosylases that have partial overlapping substrate specificities to find and remove these lesions. In human cells, repair of IR-induced base damage is carried out by at least 5 glycosylases: NTHL1, OGG1, NEIL1, NEIL2, and NEIL3 [reviewed in Baiken et al. (2020)]. As part of the initial discovery and characterization

CONTACT R. Stephen Lloyd lloydst@ohsu.edu Oregon Institute of Occupational Health Sciences, Oregon Health & Science University, Portland, OR 97239, USA

of the human gene encoding endonuclease VIII-like 1 (NEIL1) (Bandaru et al. 2002; Hazra et al. 2002; Morland et al. 2002), it was demonstrated that a 5-fold reduction in expression of *NEIL1* in TC1 embryonic stem cells resulted in a 2-fold enhancement in cytotoxicity following low-dose cesium irradiation (0 – 2.25 Gy) (Rosenquist et al. 2003). NEIL1 is a bifunctional enzyme that removes damaged DNA bases through its glycosylase activity and subsequently cleaves the DNA backbone at the resulting apurinic/apyrimidinic (AP) site via its AP lyase activity. In addition to its catalytic activities on a subset of IR-induced base lesions, such as (2,6-diamino-4-hydroxy-5-formamidopyrimidine (FapyGua), 4,6-diamino-5-formamidopyrimidine (FapyAde), thymine glycol (ThyGly), 5-hydroxy-5-methylhydantoin (5-OH-5-MeHyd), 5-hydroxycytosine (5-OH-Cyt), dihydrothymine (DH-Thy), dihydrouracil (DH-Ura), uracil glycol (UraGly), 5-hydroxyuracil (5-OH-Ura), 5-hydroxy-methyluracil (5-OH-MeUra), and urea, NEIL1 also initiates repair on DNAs containing several alkylated imidazole ring-opened purines, including aflatoxin B_1-induced AFB_1-FapyGua, and various intra- and interstrand DNA crosslinks [reviewed in McCullough et al. (2025)].

Due to NEIL1's protective role against these and other pro-mutagenic lesions, it was hypothesized that naturally occurring SNP variants of NEIL1 could increase human risk for aflatoxin-induced hepatocellular carcinoma (HCC) (Vartanian et al. 2017; Minko et al. 2019). Given that populations in South Asia experience high levels of dietary aflatoxin exposures and hepatitis B viral infections that induce oxidative stress, investigations on SNP variants of NEIL1 that occur in this region may have clinical implications. In a previous study, we analyzed the catalytic activities of the most common South Asian variants of NEIL1, including Q67K, T103A, P206L, and T278I (Zuckerman et al. 2024). While most of these variants exhibited activities and substrate specificities comparable to those of the WT NEIL1, the T103A variant exhibited greatly diminished activities on 17-mer oligodeoxynucleotides containing either site-specific ThyGly or AFB_1-FapyGua adducts (Zuckerman et al. 2024). These results were not anticipated since the T103 position within the structure of NEIL1 is very distant from the DNA binding domain and the site of catalysis, ~26 Å (Figure 1). In this study, we integrated analyses of enzymatic activity with molecular dynamics (MD) simulations to elucidate the molecular basis of the functional deficiency observed in the T103A NEIL1 variant.

2. Materials and methods

2.1. Construction of expression plasmids for mutant NEIL1 enzymes and purification

The pET22b(+) plasmid vector encoding the gene-edited form of WT NEIL1 (K242R) in frame with a C-terminal 6-histidine purification tag (Minko et al. 2020) was used as

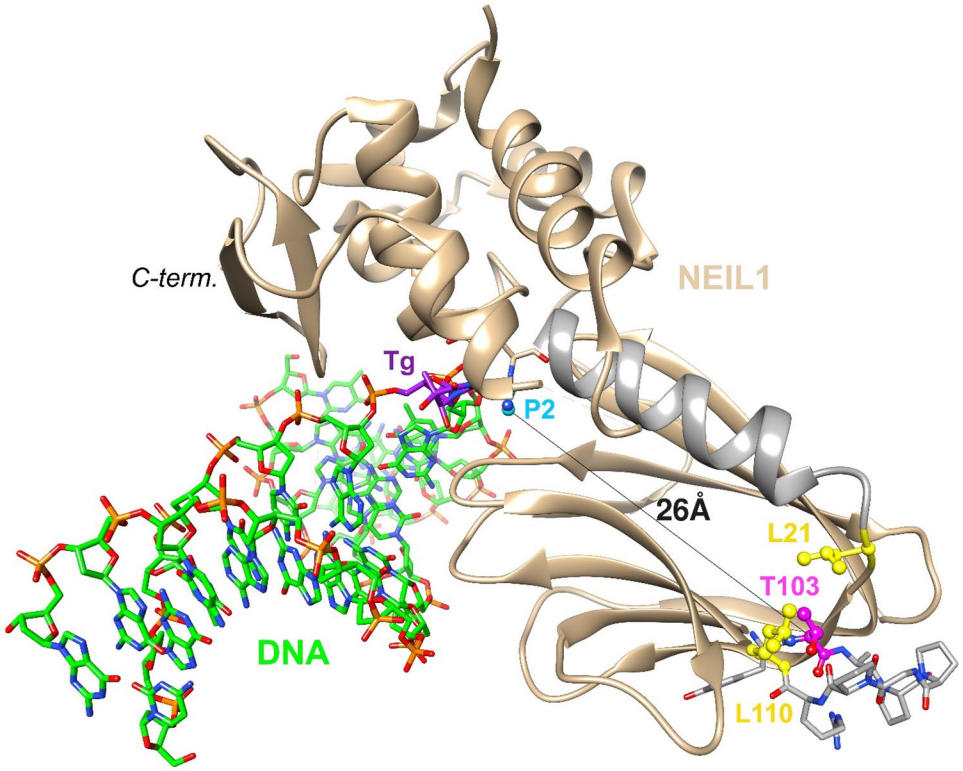

Figure 1. Crystal structure or human NEIL1 in complex with double-stranded DNA containing thymidine glycol (ThyGly) lesion (PDB ID 5ITX) (Zhu et al. 2016). NEIL1 is shown in cartoon mode and colored in tan and the DNA is colored by atom with green carbons. Carbon atoms of ThyGly at the active site are colored in purple and selected NEIL1 residues are highlighted in ball-and-stick mode and labeled: P2 (cyan), L21 (yellow), T103 (magenta) and L110 (yellow). The remaining residues of the 103–110 loop on the surface are shown with their side chains and carbons colored grey. The thin black line marks the distance between the C_α atoms of P2 and T103. The latter is wedged between L110 and L21 and the α-helix that links the latter to residues P2 and E3 at the active site is highlighted in grey.

a template. The plasmid DNAs to express the T103S and T103V NEIL1 mutants were constructed by site-directed mutagenesis following the previously described protocol (Zuckerman et al. 2024). These mutations at codon 103 were engineered using the Q5 Site-directed Mutagenesis kit (New England Biolabs) with the following primers (purchased from Integrated DNA Technologies): T103S forward (5′-TTTTACAGCGCCCCGCCTGGCCC-3′); T103S reverse (5′-GCGCAGGTGGGCATGGCGTGG-3′); T103V forward (5′-TTTTACGTGGCCCCGCCTGGCCC-3′); T103V reverse (5′-GCGCAGGTGGGCATGGCGTGG-3′). Following PCR amplification, DNAs were introduced into 5-alpha competent *E. coli* (New England Biolabs) and individual colonies were selected by overnight growth on LB plates containing 50 μg/mL ampicillin. Isolated colonies were subsequently grown in ampicillin-supplemented LB broth and plasmids were purified using QIAprep Spin Miniprep kit (Qiagen). The NEIL1 open reading frame in these plasmid DNAs was sequenced and the mutations verified by Sanger sequencing technique in the Vollum Institute DNA Sequencing Core, OHSU. Mutant NEIL1 enzymes were expressed and purified as previously described (Zuckerman et al. 2023). Pooled fractions of WT and mutant NEIL1 enzymes were estimated to be > 95% pure; these were stored at −80 °C.

2.2. Activities of WT and mutant NEIL1 on site-specifically modified oligodeoxynucleotides

DNA incision activity was measured by plate reader- and gel-based methods. These assays used duplex oligodeoxynucleotides containing site-specific lesions including ThyGly, AFB_1-FapyGua, or an AP site that was created by removal of uracil (U) by uracil DNA glycosylase (UDG). The ThyGly- and U-containing oligodeoxynucleotides were 17-mers labeled with the TAMRA fluorophore at the 5′ end (5′-(TAMRA)-TCACCT(ThyGly)CGTACGACTC-3′ and 5′-(TAMRA)-TCACC(U)TCGTACGACTC-3′). The complementary strands placed an adenine opposite ThyGly and a cytosine opposite the AP site. In real-time (plate reader–based) assays, the complementary strand was conjugated with Black Hole Quencher 2 (BHQ2) at the 3′ end. AP sites were generated by incubating 100 nM duplex U-containing DNA with 10 units of UDG (New England Biolabs) in 100 μL of standard NEIL1 reaction buffer (see below). Preparation of the 20-mer oligodeoxynucleotide containing AFB_1-FapyGua (5′-CCATA(AFB_1-FapyGua)CTACCATCGCTGGA-TAMRA-3′) was previously described (Tomar et al. 2021). All other oligodeoxynucleotides were purchased from Integrative DNA Technologies.

Glycosylase/AP lyase reactions on site-specifically modified oligodeoxynucleotides were performed in the following buffer: 20 mM Tris-HCl (pH 7.4), 100 mM KCl, 100 μg/mL BSA, and 0.01% (v/v) Tween 20. WT or mutant NEIL1 was combined with $MgCl_2$, $CaCl_2$, or $MnCl_2$, and reactions were initiated in black 384-well plates (Corning Inc.) by adding enzyme solutions to DNA substrates. Final concentrations of DNA substrates, NEIL1 enzymes, $MgCl_2$, $CaCl_2$, and $MnCl_2$ are provided in the figures or figure legends. Relative fluorescence was measured every 2 min at 37 °C on an Infinite M200 Tecan plate reader, using 525/9 nm excitation and 598/20 nm emission filters. Reaction rates during the linear phase were determined by fitting data to a linear equation and normalized to the rates of control reactions. To determine $MgCl_2$ concentrations that yield 50% of maximal enhancement (EC_{50}) or inhibition (IC_{50}) of enzymatic activity, the relative initial rates were plotted in Kaleidagraph and analyzed using AAT Bioquest calculators (https://www.aatbio.com).

For experimental designs that analyzed DNAs by electrophoretic mobility changes, reactions were conducted at 37 °C for 10 min and terminated by the addition of either 95% (v/v) formamide and 20 mM EDTA at a 1:4 ratio or the same solution containing 250 mM NaOH, following by heating at 95 °C for 2 min. Substrate and product DNAs were separated on 15% polyacrylamide gels containing 8 M urea. TAMRA-labeled DNAs were visualized using a FluorChem M system (Protein Simple) with a 534 nm LED light source and a 607/36 nm emission filter.

2.3. MD Simulations

The crystal structure for human NEIL1 (PDB code: 5ITQ) (Zhu et al. 2016) was used to generate starting coordinates for all simulations. Coordinates for surface loop residues H204, R205 and P206 are missing in the 5ITQ crystal structure. Therefore, these residues were modeled using standard backbone torsion angles and then relaxed with energy minimization to remove any residual conformational strain. To generate the T103A variant structure, the T103 surface loop residue was replaced with alanine, retaining the threonine C_β carbon atom position for the alanine C_β carbon. The T103A variant with a single Mg^{2+} cation complexed with surface loop 102-110 (Figure 1) was built using data and guidelines from previous studies (Lu et al. 2012; Piovesan et al. 2012; Khrustalev et al. 2016).

All energy minimization and molecular dynamics simulations were performed with the PMEMD AMBER module (Case et al. 2023), using the AMBER ff19SB force field for protein (Tian et al. 2020), along with the OPC water model (Izadi et al. 2014) and corresponding parameters for ions (Sengupta et al. 2021). Each protein model was solvated in a truncated octahedron box with a 14 Å buffer zone between any protein atom and the closest box wall. The starting structure was subjected to a three-step minimization procedure. First, the protein was relaxed for 10,000 steps of conjugate gradient minimization, while water molecules and counterions were restrained at starting positions. Then, all solvent molecules and ions were relaxed for 10,000 steps while the protein was restrained. Finally, all restraints were removed, and the entire system was minimized for 10,000 additional steps. The minimized complex was then heated gradually from 0 to 300 K during a 200 ns canonical ensemble (NVT) MD simulation, followed by a ~300 ns NPT ensemble simulation, using a 2 fs timestep. After this equilibration phase, all MD trajectories were propagated for 2-3 microseconds. Energy and force calculations were performed

using minimal image periodic boundary conditions with a 12 Å nonbonded cutoff for real space interactions, a homogeneity assumption to approximate the contributions of long-range Lennard-Jones forces to the virial tensor, and staggered particle-mesh Ewald for long-range electrostatics correction (Cerutti et al. 2009). A Langevin thermostat with a collision frequency of $3\,ps^{-1}$ was used to maintain the system temperature (Izaguirre et al. 2001). All covalent bonds with hydrogen atoms were constrained using the SHAKE algorithm (Ryckaert et al. 1977) and the SETTLE method was used to maintain rigid water geometry (Miyamoto and Kollman 1992). Final numerical analysis of all MD trajectories was performed using the cpptraj package (Roe and Cheatham 2013) and the ChimeraX program was used for visualization of all structures (Meng et al. 2023), with the CPK model applied for space-filling representations (Koltun 1965). After completion of the MD simulations, valine and serine residues were substituted at position T103 for multiple configurations from the WT MD simulation, to assess the potential impact of these mutations. The valine and serine substitutions, and subsequent analysis for steric clashes with the substituted residues, were automated using options in the ChimeraX program. We utilized this automated procedure to facilitate the process and also to avoid potential user bias that could be introduced with manual model building and assessment.

3. Results

3.1. Divalent cation stimulation of the catalytic efficiency of the NEIL1 T103A variant

Previously, as part of an investigation characterizing the NEIL1 variants that are primarily associated with populations in South Asia, it was demonstrated that relative to the WT NEIL1, the T103A NEIL1 variant had a reduced catalytic efficiency on 17-mer oligodeoxynucleotides containing either a ThyGly or an AP site (Zuckerman et al. 2024). This result was unanticipated due to both the relatively conservative nature of the amino acid change and its distance from the DNA binding and catalytic sites. As shown in Figure 1, the distance of the T103 residue from the active site P2 residue is ~26 Å.

Although it was established that the AP lyase activity was compromised in the T103A NEIL1 variant (Zuckerman et al. 2024), the effect of this substitution on the glycosylase activity was unknown. To address this question, we proposed to incubate ThyGly-containing oligodeoxynucleotides with the T103A variant in the presence of AP endonuclease 1 (APE1), which would cleave DNA at any residual AP sites created in the T103A-catalyzed glycosylase reaction. Since APE1 is a magnesium-dependent enzyme, we first tested whether NEIL1 activity would be affected by the addition of Mg^{2+} to the reaction buffer. Specifically, control incision reactions were performed with 50 nM WT and T103A NEIL1 in either the standard buffer or an APE1-appropriate buffer containing 10 mM $MgCl_2$ (Figure 2(A)). Surprisingly, these data demonstrated that while the WT NEIL1 was inhibited by ~40% in the presence of 10 mM $MgCl_2$, reactions containing T103A showed a ~3-fold increase in incision rates. Despite this significant increase, the rate of incision by T103A remained below that observed for WT NEIL1. The concentration of $MgCl_2$ required to decrease the maximal reaction rate of WT NEIL1 by 50% (IC_{50}) was determined to be 10.2 ± 0.2 mM (Figure 2(B)). The concentration producing a 50% increase in the maximal enhancement (EC_{50}) of T103A activity was 2.7 ± 1.8 mM (Figure 2(C)). Comparable to the decreased activity observed for WT NEIL1 at 20 and 40 mM concentrations of $MgCl_2$, the activity of the T103A variant was also reduced under these conditions.

To investigate whether other divalent cations could inhibit WT NEIL1 and stimulate the T103A variant, DNA incision reactions were performed using the ThyGly-containing oligodeoxynucleotide with $CaCl_2$ or $MnCl_2$. The rates of reactions carried out using $CaCl_2$ were equivalent with those observed for reactions with $MgCl_2$ (Figure 2(A)). Incubation in the presence of $MnCl_2$ was inhibitory to both the WT and T103A variant NEIL1 (data not shown). The products of DNA incision reactions were also analyzed using gel-based electrophoretic separation of oligodeoxynucleotides containing either ThyGly or AFB_1-FapyGua. These DNAs were incubated with different concentrations of WT and T103A NEIL1 in the presence or absence of these divalent cations, with assays performed in duplicate. These data were consistent with those reported in Figure 2, such that WT NEIL1 was inhibited by all tested divalent cations and the T103A variant was stimulated by $MgCl_2$ and $CaCl_2$ (data not shown).

To test the effects of these metals on the DNA glycosylase step, the experimental design was changed to distinguish glycosylase alone vs combined glycosylase/AP lyase activities. Specifically, WT and T103A NEIL1 were assayed in duplicate in the presence or absence of divalent cations, with residual AP sites detected following conversion of these sites into DNA strand breaks by incubation with NaOH (data not shown). These data revealed that the T103A NEIL1 variant was compromised in not only its AP lyase activity, but also its glycosylase activity, both of which are restored in the presence of $MgCl_2$.

To further investigate the basis of the T103A functional deficiency, the amino acid at position T103 was changed to encode serine (S) or valine (V). The rationale for the changes was guided by analyses of the local environment surrounding T103. Replacement of T by S or V does not affect side-chain volume and favorable steric interactions to the same extent as replacement of T by A. Rather, these substitutions were designed to probe the effect of the balance between electrostatic and nonpolar interactions by comparing S (H-bond), T (H-bond and nonpolar), and V (nonpolar) at position 103. Following purification, the catalytic activities of the T103S and T103V mutant proteins were measured using the ThyGly-containing oligodeoxynucleotide (Figure 3). These data demonstrated that the activity of the T103S NEIL1 mutant was significantly reduced relative to WT ($p < .001$). The stimulatory effects of 10 mM $MgCl_2$ and $CaCl_2$ were observed in this mutant, with an ~2.5-fold stimulation for both cations. The activity of T103V NEIL1 mutant was comparable in the presence or absence of 10 mM cations.

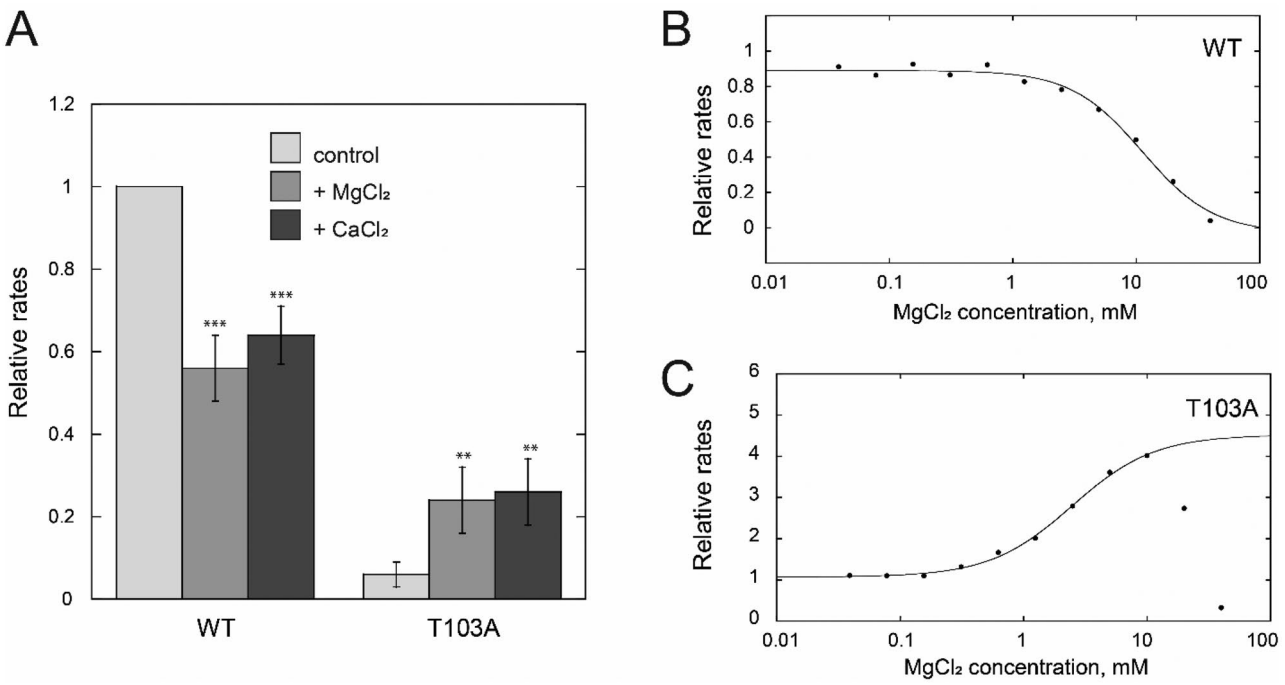

Figure 2. Changes in the rates of combined glycosylase/AP lyase activities of the WT and T103A NEIL1 in the presence of $MgCl_2$ or $CaCl_2$. Relative reaction rates were measured at 37 °C in three independent experiments using 50 nM ThyGly-containing oligodeoxynucleotides and 50 nM enzymes. (A) Reactions were performed in NEIL1 reaction buffer without or with 10 mM $MgCl_2$ or $CaCl_2$. Relative rates were compared for each enzyme in the presence of $MgCl_2$ or $CaCl_2$ versus standard reaction conditions (** = $p < .01$; *** = $p < .001$). (B) IC_{50} values for inhibition of the WT NEIL1 were determined using the range of concentrations of $MgCl_2$ from 0.039 to 40 mM. **C**. For the T103A NEIL1 variant, reactions were conducted using the range of concentrations of $MgCl_2$ from 0.039 to 40 mM, and EC_{50} values were calculated using concentrations from 0.039 to 10 mM.

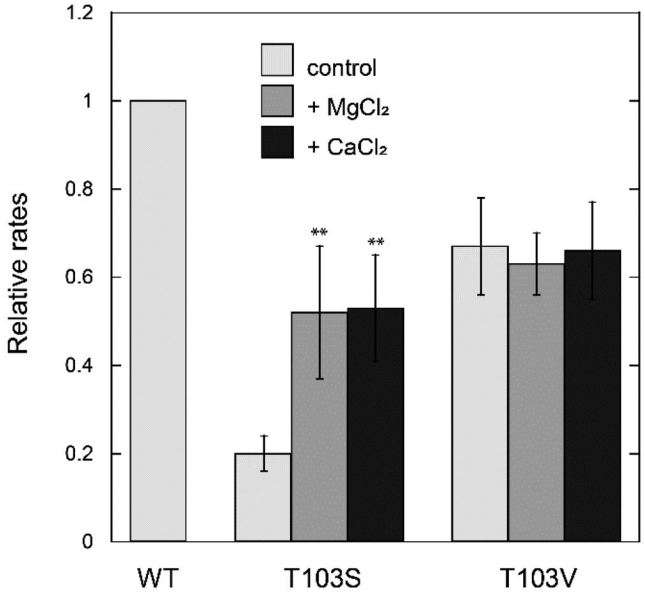

Figure 3. Changes in the rates of combined glycosylase/AP lyase activities of the T103S and T103V NEIL1 mutants in the presence of $MgCl_2$ or $CaCl_2$. Relative reaction rates were measured at 37 °C in three independent experiments using 50 nM ThyGly-containing oligodeoxynucleotides and 50 nM enzymes. Reactions were performed in NEIL1 reaction buffer without or with 10 mM $MgCl_2$ or $CaCl_2$. Relative rates were compared for each enzyme in the presence of $MgCl_2$ or $CaCl_2$ versus standard reaction conditions (** = $p < .01$).

3.2. MD Simulations

The MD simulations not only display many similarities for the WT, the T103A variant, and the T103A variant with Mg^{2+} cation systems, but also reveal some dramatic differences in behavior for the three systems. The surface loop 102-110 exhibited a comparable range of motion for all three systems (Figure 4(A)), with Root Mean Square Deviation (RMSD) values of ~0.75 Å. However, while each system sampled comparable regions of conformational space, the T103A variant loop had higher structural fluctuation values (Figure 4(B)), indicating increased dynamics or flexibility. The structural fluctuation values for the 102-110 loop in the system with Mg^{2+} were more variable, but were computed using a far smaller number of configurations (~10^3) versus the WT or T103A variant NEIL1 simulations with no Mg^{2+} (~10^6 configurations for each). This is because the Mg^{2+} interaction with the 102-110 loop was weak and transient, persisting for only a few hundred nanoseconds at most. The Mg^{2+}-loop interaction is weak because the cation is not chelated directly by the loop backbone carbonyl groups, but rather interacts with the loop as a cation-hexahydrate complex ($Mg^{2+}(H_2O)_6$) (Figure 4(C-a)). Figure 4(C-b) presents a snapshot from the MD trajectory illustrating weak cation coordination with carbonyl oxygens from residues A104, P106, and P108 in the 102-110 surface loop, as well as residue V22 near the end of α-helix 2-20.

While the behavior for surface loop 102-110 is reasonably similar in all three simulations, we observe dramatically different behavior in the active site region for each complex. We monitored the behavior of five active site residues: P2, E3, E6, M81 and Y244, as these residues are either crucial for catalytic activity (e.g., P2 and E3) or have been documented to make important contacts with ligands (Zhu et al. 2016; Lloyd 2022; Tomar et al. 2023). Table 1 presents

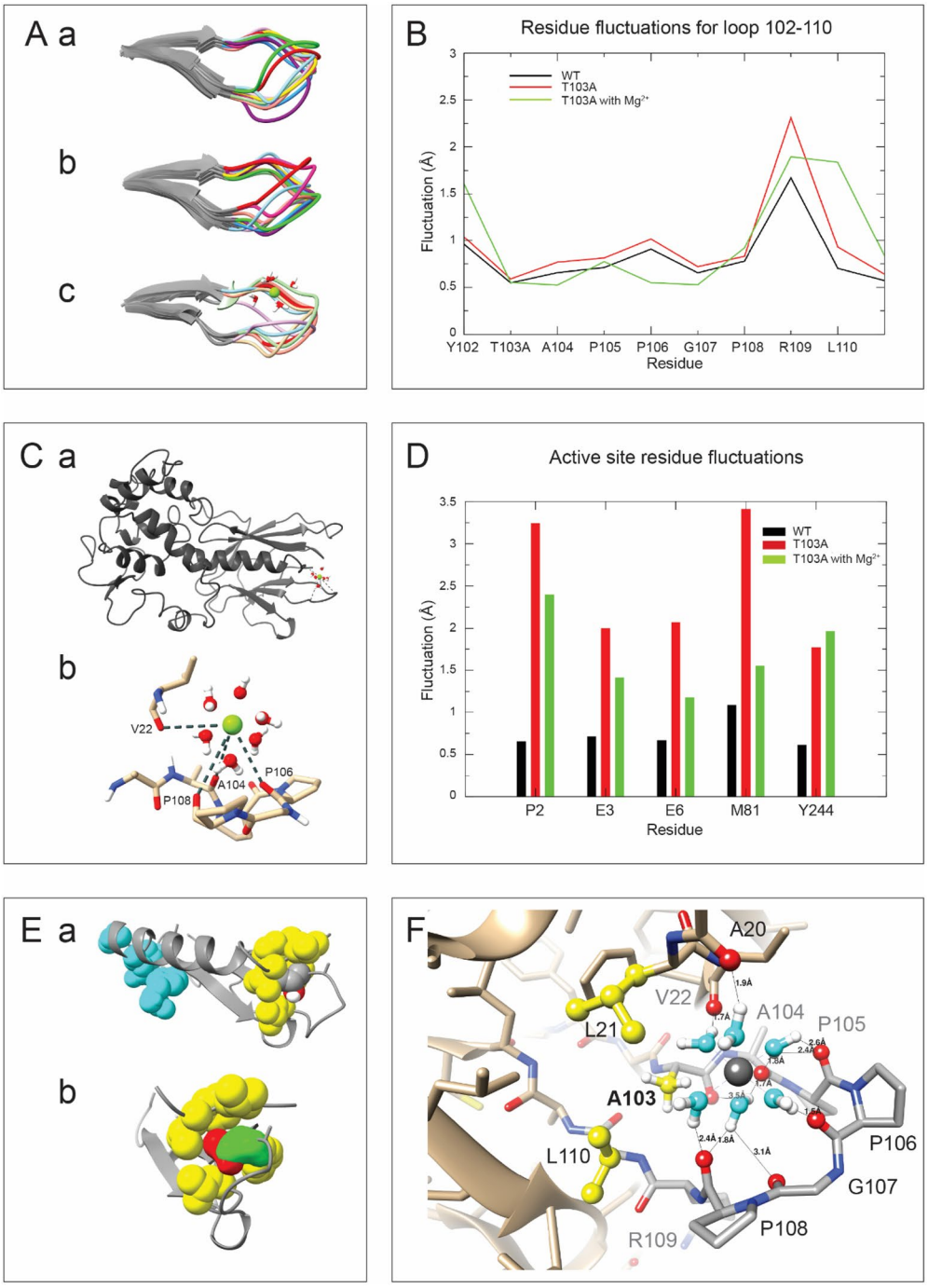

Figure 4. Molecular dynamic simulations. (A) Snapshots of loop 102-110 from molecular dynamics simulations for a. WT enzyme, b. T103A variant, and c. T103A variant with Mg^{2+}. Each colored loop conformation represents an MD simulation configuration at 200 nanosecond intervals. In Panel A-c, the Mg^{2+} hexahydrate complex is bound to the loop. (B) Structural fluctuations for loop 102-110 residues during the final 2 microseconds of each MD simulation. Note that data sampling for the T103A variant with Mg^{2+} is extremely limited because of the transient nature of the cation-loop interaction, due to weak cation binding. As a result, the fluctuation values for the T103A variant in the presence of Mg^{2+} have lower confidence. (C) Snapshot of the T103A variant complexed with a Mg^{2+}. (a) Overview of the enzyme rendered as a grey ribbon structure with the Mg^{2+} hexahydrate complex bound to the 102-110 surface loop. Mg^{2+} is rendered as a green sphere, and waters are rendered as red and white ball-and-stick structures. (b) Detailed view of the Mg^{2+}-$(H_2O)_6$ interactions with surface loop residues. Dashed grey lines highlight interactions between carbonyl groups of loop residues A104, P106 and P108, as well as an interaction with the carbonyl group of V22, located near the end of α-helix 2-20 as shown in Panel C-a. (D) Structural fluctuations for active site residues P2, E3, E6, M81 and Y244 during the final 2 microseconds of each MD simulation. As noted for Panel B, the fluctuation values for the T103A variant with Mg^{2+} have lower confidence because of limited sampling due to the transient nature of the enzyme-cation interaction. (E) MD simulation snapshot illustrating the enzyme active site relationship with the mutation site in loop 102-110. (a) Spatial relationship between active site residues (rendered as cyan CPK structures) and T103 (rendered as grey/red/white CPK structure) in the 102-110 surface loop. The active site and loop are "coupled" by α-helix 2-20 and a β-sheet composed of residues 83-88/99-102/111-116, depicted as grey ribbon structures. (b) Detailed view of the T103A mutation site in loop 102-110. The green surface displays the volume occupied by the smaller alanine side chain at position 103. The red surface illustrates the larger volume occupied by the WT threonine side chain at this position (the threonine volume includes all of the green and red surface). Residues from the end of α-helix 2-20 and the edge of the β-sheet are rendered as yellow CPK structures and display the close packing contacts formed with the WT threonine, as well as the void formed when an alanine residue is substituted at this position. (F) Close-up view of the NEIL1 surface loop encompassing residues 103 to 110 depicting the energy-minimized pose of Mg^{2+} hexahydrate coordinated to several backbone oxygen atoms. Loop carbon, nitrogen and oxygen atoms are colored in grey, blue and red, respectively, the grey sphere in the center is Mg^{2+}, water molecules are shown in ball-and-stick mode with oxygen and hydrogen atoms colored in cyan and white, respectively, and the L21, A103 and L110 side chains are highlighted in yellow. Thin solid lines indicate the distances between water H-atoms and backbone oxygens and the Mg^{2+} coordination sphere is shown with dashed lines.

Table 1. Root Mean Square Deviation values for active site residues P2, E3, E6, M81 and Y244.

NEIL1	Backbone (N, C_{α}, C)	Backbone + Side Chain
WT	0.48 Å ± 0.13 Å	1.19 Å ± 0.20 Å
T103A	3.12 Å ± 1.26 Å	3.95 Å ± 1.03 Å
T103A + Mg^{2+}	1.95 Å ± 0.93 Å	2.32 Å ± 1.01 Å

RMSD data for these active site residues which show that the active site in the WT enzyme is extremely stable over the entire trajectory, with only small fluctuations from the crystallographic positions. In dramatic contrast, the T103A variant NEIL1 displays large structural deviations over the simulation, with frequent major disruptions of the overall active site geometry. The active site residue fluctuations, i.e., dynamic motion, are also much larger for the T103A variant (Figure 4(D)). The behavior of the T103A variant when Mg^{2+} is added to the system is intermediate between that of WT enzyme and the variant without Mg^{2+}. The Mg^{2+} interactions with the 102-110 surface that was discussed above (Figure 4(B)), appear to stabilize the enzyme active site to some extent.

4. Discussion

4.1. Initial report of a divalent metal cation-stimulated glycosylase variant

While magnesium is essential for many catalytic reactions within the BER pathway, including those involving AP endonucleases such as APE1, DNA polymerases β and δ, and DNA ligases, this is not the case for most DNA glycosylases. Throughout the initial discoveries and characterizations of DNA glycosylases, reaction conditions containing metal-chelating agents were routinely optimized for factors such as salt concentrations, pH range, and temperature. Although there were subtle differences in each enzyme's optimal reaction conditions, activities of these enzymes were generally not inhibited by chelating agents, suggesting that divalent metal cations were not essential for catalysis. These findings held true for the four iron-four sulfur (4Fe-4S) cluster-containing glycosylases such as MutY and Nth1 (Manuel and Lloyd 1997; Dizdaroglu et al. 1999). Furthermore, lack of either stimulation or inhibition of NEIL1 by 500 nM $MgCl_2$ was directly demonstrated (Hegde et al. 2010). However, an exception to this general conclusion has been shown for the human DNA glycosylases, hUNG2 and hSMUG1, for the removal of uracil in single-stranded DNA and from U:A and U:G mismatches (Kavli et al. 2002).

In this study, to further characterize the enzymatic deficiencies of the T103A NEIL1 variant, we conducted the reactions in the presence of divalent metal cations and demonstrated that the activity of this enzyme was significantly enhanced by magnesium and calcium. In contrast, manganese was inhibitory to both the WT NEIL1 and T103A variant. In this regard, the Mitra laboratory had reported inhibition of NEIL1 by 500 nM $CuCl_2$, $FeSO_4$, $FeCl_3$, and $AlCl_3$ (Hegde et al. 2010). For Fe(II/III) and Cu(II), these metals were shown to bind directly to NEIL1, thereby inhibiting catalysis and disrupting protein-protein interactions. It has also been demonstrated that inhibition of NEIL1 by Cu^{2+} and Cd^{2+} occurs through the formation of metal-DNA complexes that interfere with damage recognition (Grin et al. 2009). Although not explicitly tested here, our data on manganese-mediated inhibition of NEIL1 could be consistent with either mechanism.

The structure of NEIL1 does not map to any of the human protein clusters that feature Mg^{2+} binding sites (Piovesan et al. 2012). Moreover, the glycosylase does not contain a predominant secondary structural motif that is characteristic of Mg^{2+} or Mn^{2+} coordination sites (Khrustalev et al. 2016), nor does it contain Asp and/or Glu residues in close spatial proximity that are indicative of Mg^{2+} or Ca^{2+} binding sites (Lu et al. 2012). However, Mg^{2+} binding to the NEIL1 loop described here differs from the above motifs and Asp/Glu-dominated Mg^{2+} binding sites at active sites of nucleic acid-processing enzymes such as polymerases, endonucleases, and exonucleases. Thus, the interaction is more dynamic and features exclusively water-mediated contacts unlike at enzyme active sites that display inner-sphere coordination by Mg^{2+}.

Mg^{2+} and Ca^{2+} exhibit different DNA binding modes and result in distinct consequences for duplex conformation and packing. We analyzed Mg^{2+} and Ca^{2+} binding to the Dickerson-Drew Dodecamer (DDD) B-form DNA of sequence 5′-CGCGAATTCGCG-3′ using X-ray crystallography at atomic resolution (Minasov et al. 1999). The crystal structures of the DDD in the presence of the two alkaline earth metal ions are non-isomorphous and offer the most detailed picture of the ionic environment of B-DNA. Individual duplexes in the magnesium and calcium crystal forms are surrounded by 13 Mg^{2+} and 11 Ca^{2+} ions, respectively. The metal ions trigger different end-to-end contacts between adjacent DDDs as well as lateral contacts. A Mg^{2+} ion sits in the major groove near one end of the duplex and stabilizes a distinct kink at that site. At the minor groove periphery, Mg^{2+} ions bridge phosphate groups from opposite strands and cause a narrowing of the groove at the edge of the central A-tract. Conversely, Ca^{2+} resides inside the minor groove and contacts base edges via its hydration shell. All Mg^{2+} ions are hexacoordinated and display the well-known, strict octahedral coordination geometry. By comparison, Ca^{2+} ions show a more irregular geometry, and some are hexacoordinated and others heptacoordinated. In addition to residing inside opposite grooves, Ca^{2+} ions form more inner-sphere complexes than Mg^{2+} ions, in-line with the lower hydration enthalpy of Ca^{2+} compared to Mg^{2+}. Given these distinct metal-binding modes, our observation that Mg^{2+} and Ca^{2+} interchangeably rescue the activity of the T103A NEIL1 variant is not likely attributed to the direct binding of the ions to DNA. Instead, a relatively loose binding mode of the two ions to the NEIL1 loop, based exclusively on water-mediated contacts and no inner-sphere coordination, better fits the T103A NEIL1 variant activity profile. Moreover, despite similar binding modes of the two metal ions at active sites of DNA- or RNA-processing enzymes, Mg^{2+} is conducive to activity whereas Ca^{2+} typically is not. Even when Ca^{2+} does act as a cofactor of a

reaction such as *S. solfataricus* Dpo4-catalyzed DNA polymerization, it cannot fully replace Mg^{2+}. Thus, Ca^{2+} is an inhibitor of the Dpo4 pyrophosphorolysis activity (Irimia et al. 2006).

4.2. Potential structural basis of the metal-stimulated activities associated with T103A

It seems plausible that the large structural fluctuations and highly dynamic nature of the T103A active site observed in the MD simulations can explain the reduced catalytic activity of this variant. The relative active site structural stabilization observed when a magnesium cation is present is likely due to the weak, transient Mg^{2+} interaction with the 102-110 surface loop, as presented above. This relative structural stabilization is consistent with the experimental observation that Mg^{2+} addition only partially rescues enzymatic activity. Based on our simulation results, we predict that increasing the Mg^{2+} concentration in the MD simulation might enhance active site stabilization and presumably, enzymatic activity, through a simple mass action effect. Specifically, higher Mg^{2+} concentrations increase the probability of productive interactions between the cation and the 102-110 surface loop. This prediction is consistent with the experimental results which demonstrate a cation concentration-dependent catalytic rescue effect.

The correlation between the 102-110 surface loop dynamic behavior and the active site dynamics observed in our simulations is dramatic. While our current data do not enable us to propose a detailed mechanism for the coupling of the T103A mutation site with the enzyme active site, the crystal structure (Figure 1) and snapshots collected from our MD trajectories provide a plausible general explanation. Figure 4(E) shows a portion of the enzyme structure, highlighting the active site residues (depicted as cyan CPK structures) and the 102-110 surface loop with T103 presented as a multi-colored CPK structure. As this figure shows, this surface loop and the active site are physically connected, and we propose, are mechanically coupled to each other, via α-helix 2-20, as well as a β-sheet formed by residues 83-88/99-102/111-116. In the WT enzyme, T103 forms tight, favorable packing interactions and a H-bond with residues near the C-terminus of the α-helix, including L21 and V22 (highlighted as a yellow CPK structure), as well as residues near or at the edge of the β-sheet, including F23, L87, Y102 and L110 (displayed as yellow CPK structures). When the much smaller alanine residue is substituted for threonine in the T103A variant, it creates a cavity or void at this interface and the tight packing interactions are disrupted, as shown in Figure 4(F), and the H-bond is lost. This disruption of the tight packing contacts and the H-bond interaction explains the increased loop structural fluctuations we observe for the T103A NEIL1 variant. We propose that the increased structural dynamics at the interface of the surface loop (mutation site) with the α-helix and β-sheet gets transmitted to the enzyme active site, leading to increased dynamics there, with a concomitant loss of enzymatic activity. Additional experiments and simulations will be needed to probe this proposed coupling mechanism in greater detail.

As pointed out for the T103A NEIL1 variant, the alanine side chain is too short for favorable packing interactions with adjacent side chains. Also, the H-bond between threonine OH and the L110 amide moiety, which is observed in the crystal structure of WT NEIL1 is lost. Based on analysis of the WT crystal structure, the T103S NEIL1 mutant can in principle preserve the H-bond, but the lack of the methyl group of the serine side chain disrupts the favorable packing interactions. However, the T103V NEIL1 mutant should maintain favorable packing interactions with L21 and L110 side chains. To test these hypotheses more rigorously, we used an automated modeling protocol to substitute valine or serine at position T103 for multiple snapshots from the WT MD simulations. The rationale for this exercise was simple: if valine is indeed a good substitute for threonine at position 103, it should "fit" well in snapshots from the WT simulation without adjustment or structure relaxation. The results show that valine can be accommodated in ~90% of all tested configurations from the WT MD trajectory with excellent side chain packing. The remaining 10% of tested configurations exhibited extremely minor steric clashes, involving aliphatic hydrogen-hydrogen contact distances that were 0.1–0.2 Å too short, based on the default van der Waals parameters used by ChimeraX. As expected from the crystal structure analysis, the serine residue is too small to maintain favorable side chain packing interactions. We also observed that the shorter serine side chain fails to maintain favorable H-bond interactions with the L110 amide backbone, or any other enzyme residues, in most MD snapshots tested. In essence, the serine residue appears to behave very much like alanine at position 103, which is consistent with the experimental results. These modeling results, together with the experimental observation that T103V activity does not display Mg^{2+} dependence, unlike either T103A or T103S, strongly suggests that maintaining favorable side chain packing interactions at position 103 is more important for loop dynamics and enzyme activity than preserving an H-bond with L110. A more detailed analysis of H-bonding patterns in the WT MD simulation reveals that the T103 H-bond with L110 is only present ~70% of the time, and is disrupted regularly by water molecules, further supporting the idea that H-bonding by T103 is less important for structural stabilization than is favorable side chain packing. Together, these MD simulation and modeling results suggest that T103 mutations cause side-chain dependent changes in the dynamic behavior of the loop, leading to the unusual metal ion dependence of a glycosylase arising because Mg^{2+} can partially restrain the increased loop flexibility caused by the T103A and T103S mutations.

Based on the MD simulations, we speculate that magnesium and calcium are not directly involved in the enzyme's chemistry, but instead, these cations induce conformational changes in the T103A variant, facilitating damage recognition, nucleotide flipping, and subsequent catalysis. These mechanisms are also likely to account for the prior observations that, in the absence of magnesium, the catalytic activity of the T103A variant increased with DNA substrate

length such that incision of a 51-mer oligodeoxynucleotide containing ThyGly was only about 8-fold reduced relative to WT NEIL1, and the rates of base excision from genomic DNA was indistinguishable between the two enzymes (Zuckerman et al. 2024). Thus, we consider that in the absence of metals, general salt-dependent, nonspecific DNA binding may induce similar stabilization in the T103A variant, thus improving catalytic activity which on short DNAs can only be achieved via metal binding.

4.3. Implications for human health and disease risk

Our prior investigations characterizing the SNP variants of NEIL1 suggested that reduced catalytic efficiency of the T103A NEIL1 variant could potentially elevate disease risk in humans, especially in contexts involving aflatoxin exposures and viral hepatitis infections (Zuckerman et al. 2024). The present investigation has provided greater insights into the conditions in which this SNP variant remains functional. In the presence of physiologically relevant magnesium concentrations, the T103A NEIL1 variant appears to possess the same range of substrate recognition as the WT, albeit with reduced catalytic efficiency using oligodeoxynucleotide substrates. Collectively, these data suggest that further investigations on the pathogenicity of the T103A NEIL1 variant is warranted.

Acknowledgements

The authors want to especially acknowledge the integral role of Dr. Miral Dizdaroglu and his exceptionally talented associates, Drs. Pawel Jaruga and Melis Kant in the initial characterization of many of the SNP variants of NEIL1, especially the T103A variant. Dr. Dizdaroglu's boundless enthusiasm for pushing the boundaries of knowledge in the DNA repair field was inspirational to us all. We will genuinely miss these opportunities and collaborations with his passing.

Author contributions

CRediT: **Jamie T. Zuckerman**: Investigation, Writing – original draft; **Irina G. Minko**: Formal analysis, Investigation, Visualization, Writing – review & editing; **Terry P. Lybrand**: Formal analysis, Investigation, Visualization, Writing – review & editing; **Martin Egli**: Conceptualization, Formal analysis, Funding acquisition, Visualization, Writing – review & editing; **Amanda K. McCullough**: Conceptualization, Funding acquisition, Writing – review & editing; **R. Stephen Lloyd**: Conceptualization, Funding acquisition, Writing – original draft, Writing – review & editing.

Disclosure statement

No potential conflict of interest was reported by the author(s).

Funding

This work was supported by National Institutes of Health (NIH) grants R01 CA-55678, R01 ES-029357, and P01 CA-160032 (M.E, A.K.M., and R.S.L.). The Vanderbilt-Ingram Cancer Center is funded by NIH grant P30 CA-068485. R.S.L. and AKM acknowledge support from the National Institute of Environmental Health Sciences (R01 ES-031086) and from the Oregon Institute of Occupational Health Sciences at Oregon Health & Science University via funds from the Division of Consumer and Business Services of the State of Oregon (ORS 656.630). Funding for open access charge: NIH.

Notes on contributors

JTZ was a Research Assistant 2 at Oregon Health & Science University, where she performed biochemical characterization of pathogenic variants of DNA glycosylases. She is currently a Ph.D. student in the Molecular and Cellular Biology program at the University of Washington. There, she studies regulatory factors of kinetochore assembly and function, hoping to gain understanding of chromosome segregation errors in the context of disease, and more broadly the fundamental processes of cell division.

IGM is a researcher at Oregon Health & Science University, where she studies the molecular mechanisms that preserve genome stability. Her work centers on the biochemistry of DNA repair and replication, with a particular focus on the genotoxic and mutagenic effects of DNA-damaging agents and the cellular pathways that mitigate harmful consequences of DNA damage. Her research provides insights relevant to cancer biology, aging, and the development of targeted therapeutic strategies.

TPL is an adjoint professor at Vanderbilt University. His research involves computational studies of biomacromolecules and biomolecular complexes, with particular focus on protein-nucleic acid interactions that are relevant to gene expression and regulation processes, as well as enzyme-ligand complexes of biomedical significance. His work provides insight for biomolecular recognition processes and has applications in computer-aided, structure-based drug design projects.

ME is the Richard Armstrong Chair Professor of Innovation in Biochemistry at Vanderbilt University. His research interests include the 3D structures of DNA, RNA, and artificial pairing systems (XNA), chemical modification and conjugation of siRNA therapeutics, trans-lesion DNA polymerase-DNA adduct interactions, the structure and function of circadian clocks, the structure and activity of steroidogenic cytochrome P450s, and SAR of protein/enzyme-ligand interactions.

AKM is a Professor of Molecular & Medical Genetics at Oregon Health & Science University. Her research is focused on translating fundamental discoveries on cellular DNA damage response pathways into actionable clinical interventions and improved therapeutic responses.

RSL is a Professor at Oregon Health & Science University, with the focus of his research being in the areas of DNA repair and mutagenesis as they apply to limiting carcinogenesis, metabolic syndrome, and neurodegeneration.

ORCID

Jamie T. Zuckerman http://orcid.org/0000-0001-5719-0317
Irina G. Minko http://orcid.org/0000-0002-0012-2265
Terry P. Lybrand http://orcid.org/0000-0002-2248-104X
Martin Egli http://orcid.org/0000-0003-4145-356X
Amanda K. McCullough http://orcid.org/0000-0002-9500-4973
R. Stephen Lloyd http://orcid.org/0000-0001-7273-372X

References

Averbeck D, Rodriguez-Lafrasse C. 2021. Role of mitochondria in radiation responses: epigenetic, metabolic, and signaling impacts. Int J Mol Sci. 22(20):11047. https://doi.org/10.3390/ijms222011047

Baiken Y et al. 2020. Role of base excision repair pathway in the processing of complex DNA damage generated by oxidative stress and anticancer drugs. Front Cell Dev Biol. 8:617884. https://doi.org/10.3389/fcell.2020.617884

Bandaru V, Sunkara S, Wallace SS, Bond JP. 2002. A novel human DNA glycosylase that removes oxidative DNA damage and is homologous to *Escherichia coli* endonuclease VIII. DNA Repair (Amst). 1(7):517–529. https://doi.org/10.1016/s1568-7864(02)00036-8

Becker D, Adhikary A, Sevilla MD. 2010. Physicochemical mechanisms of radiation-induced DNA damage. In: Hatano Y, Katsumura Y, Mozumder A, editors. Charged particle and photon interactions with matter: recent advances, applications, and interfaces. CRC Press, Taylor and Francis Group. p. 503–541. https://doi.org/10.1201/b10389

Becker D, Kumar A, Adhikary A, Sevilla MD. 2020. Gamma- and ion-beam DNA radiation damage: theory and experiment. In: Dizdaroglu M, Lloyd RS, editors. DNA damage, DNA Repair and Disease: volume 2. The Royal Society of Chemistry. p. 426–457. https://doi.org/10.1039/9781839162541-00426

Case DA et al. 2023. AmberTools. J Chem Inf Model. 63(20):6183–6191. https://doi.org/10.1021/acs.jcim.3c01153

Cerutti DS, Duke RE, Darden TA, Lybrand TP. 2009. Staggered Mesh Ewald: an extension of the Smooth Particle-Mesh Ewald method adding great versatility. J Chem Theory Comput. 5(9):2322–2338. https://doi.org/10.1021/ct9001015

Dizdaroglu M, Karahalil B, Sentürker S, Buckley TJ, Roldán-Arjona T. 1999. Excision of products of oxidative DNA base damage by human NTH1 protein. Biochemistry. 38(1):243–246. https://doi.org/10.1021/bi9819071

Goodhead DT. 1994. Initial events in the cellular effects of ionizing radiations: clustered damage in DNA. Int J Radiat Biol. 65(1):7–17. https://doi.org/10.1080/09553009414550021

Grin IR, Konorovsky PG, Nevinsky GA, Zharkov DO. 2009. Heavy metal ions affect the activity of DNA glycosylases of the Fpg family. Biochemistry (Mosc). 74(11):1253–1259. https://doi.org/10.1134/s000629790911011x

Hazra TK et al. 2002. Identification and characterization of a human DNA glycosylase for repair of modified bases in oxidatively damaged DNA. Proc Natl Acad Sci U S A. 99(6):3523–3528. https://doi.org/10.1073/pnas.06205379999/6/3523[pii]

Hegde ML et al. 2010. Specific inhibition of NEIL-initiated repair of oxidized base damage in human genome by copper and iron: potential etiological linkage to neurodegenerative diseases. J Biol Chem. 285(37):28812–28825. https://doi.org/10.1074/jbc.M110.126664

Irimia A et al. 2006. Calcium is a cofactor of polymerization but inhibits pyrophosphorolysis by the *Sulfolobus solfataricus* DNA polymerase Dpo4. Biochemistry. 45(19):5949–5956. https://doi.org/10.1021/bi052511+

Izadi S, Anandakrishnan R, Onufriev AV. 2014. Building water models: a different approach. J Phys Chem Lett. 5(21):3863–3871. https://doi.org/10.1021/jz501780a

Izaguirre JA, Catarello DP, Wozniak JM, Skeel RD. 2001. Langevin stabilization of molecular dynamics. J Chem Phys. 114(5):2090–2098. https://doi.org/10.1063/1.1332996

Kavli B et al. 2002. hUNG2 is the major repair enzyme for removal of uracil from U: a matches, U: g mismatches, and U in single-stranded DNA, with hSMUG1 as a broad specificity backup. J Biol Chem. 277(42):39926–39936. https://doi.org/10.1074/jbc.M207107200

Khrustalev VV, Barkovsky EV, Khrustaleva TA. 2016. Magnesium and manganese binding sites on proteins have the same predominant motif of secondary structure. J Theor Biol. 395:174–185. https://doi.org/10.1016/j.jtbi.2016.02.006

Koltun WL. 1965. Precision space-filling atomic models. Biopolymers. 3(6):665–679. https://doi.org/10.1002/bip.360030606

Lloyd RS. 2022. Complex Roles of NEIL1 and OGG1: insights Gained from Murine Knockouts and Human Polymorphic Variants. DNA (Basel). 2(4):279–301. https://doi.org/10.3390/dna2040020

Lu CH, Lin YF, Lin JJ, Yu CS. 2012. Prediction of metal ion-binding sites in proteins using the fragment transformation method. PLoS One. 7(6):e39252. https://doi.org/10.1371/journal.pone.0039252

Manuel RC, Lloyd RS. 1997. Cloning, overexpression, and biochemical characterization of the catalytic domain of MutY. Biochemistry. 36(37):11140–11152. https://doi.org/10.1021/bi9709708

McCullough AK et al. 2025. Role of NEIL1 in genome maintenance. DNA Repair (Amst). 148:103820. https://doi.org/10.1016/j.dnarep.2025.103820

Meng EC et al. 2023. UCSF ChimeraX: tools for structure building and analysis. Protein Sci. 32(11):e4792. https://doi.org/10.1002/pro.4792

Minasov G, Tereshko V, Egli M. 1999. Atomic-resolution crystal structures of B-DNA reveal specific influences of divalent metal ions on conformation and packing. J Mol Biol. 291(1):83–99. https://doi.org/10.1006/jmbi.1999.2934

Minko IG et al. 2020. Recognition of DNA adducts by edited and unedited forms of DNA glycosylase NEIL1. DNA Repair (Amst). 85:102741. https://doi.org/10.1016/j.dnarep.2019.102741

Minko IG et al. 2019. Characterization of rare NEIL1 variants found in East Asian populations. DNA Repair (Amst). 79:32–39. https://doi.org/10.1016/j.dnarep.2019.05.001

Miyamoto S, Kollman PA. 1992. Settle: an analytical version of the SHAKE and RATTLE algorithm for rigid water models. J Comput Chem. 13(8):952–962. https://doi.org/10.1002/jcc.540130805

Morland I et al. 2002. Human DNA glycosylases of the bacterial Fpg/MutM superfamily: an alternative pathway for the repair of 8-oxoguanine and other oxidation products in DNA. Nucleic Acids Res. 30(22):4926–4936. https://doi.org/10.1093/nar/gkf618

Piovesan D, Profiti G, Martelli PL, Casadio R. 2012. The human "magnesome": detecting magnesium binding sites on human proteins. BMC Bioinformatics. 13 Suppl 14(Suppl 14):S10. https://doi.org/10.1186/1471-2105-13-S14-S10

Rezaee M, Adhikary A. 2024. The effects of particle LET and fluence on the complexity and frequency of clustered DNA damage. DNA (Basel). 4(1):34–51. https://doi.org/10.3390/dna4010002

Roe DR, Cheatham TE3rd. 2013. PTRAJ and CPPTRAJ: software for processing and analysis of molecular dynamics trajectory data. J Chem Theory Comput. 9(7):3084–3095. https://doi.org/10.1021/ct400341p

Rosenquist TA et al. 2003. The novel DNA glycosylase, NEIL1, protects mammalian cells from radiation-mediated cell death. DNA Repair (Amst). 2(5):581–591. https://doi.org/10.1016/s1568-7864(03)00025-9

Ryckaert J-P, Ciccotti G, Berendsen HJC. 1977. Numerical integration of the cartesian equations of motion of a system with constraints: molecular dynamics of n-alkanes. Comput Phys. 23(3):327–341. https://doi.org/10.1016/0021-9991(77)90098-5

Sengupta A, Li Z, Song LF, Li P, Merz KMJr. 2021. Parameterization of monovalent ions for the OPC3, OPC, TIP3P-FB, and TIP4P-FB water models. J Chem Inf Model. 61(2):869–880. https://doi.org/10.1021/acs.jcim.0c01390

Tian C et al. 2020. ff19SB: amino-acid-specific protein backbone parameters trained against quantum mechanics energy surfaces in solution. J Chem Theory Comput. 16(1):528–552. https://doi.org/10.1021/acs.jctc.9b00591

Tomar R et al. 2021. DNA sequence modulates the efficiency of NEIL1-catalyzed excision of the aflatoxin B_1-induced formamidopyrimidine guanine adduct. Chem Res Toxicol. 34(3):901–911. https://doi.org/10.1021/acs.chemrestox.0c00517

Tomar R et al. 2023. Base excision repair of the N-(2-deoxy-d-erythro-pentofuranosyl)-urea lesion by the hNEIL1 glycosylase. Nucleic Acids Res. 51(8):3754–3769. https://doi.org/10.1093/nar/gkad164

Vartanian V et al. 2017. NEIL1 protects against aflatoxin-induced hepatocellular carcinoma in mice. Proc Natl Acad Sci U S A. 114(16):4207–4212. https://doi.org/10.1073/pnas.1620932114

Ward JF. 1988. DNA damage produced by ionizing radiation in mammalian cells: identities, mechanisms of formation, and reparability. Prog Nucleic Acid Res Mol Biol. 35:95–125. https://doi.org/10.1016/s0079-6603(08)60611-x

Zhu C et al. 2016. Tautomerization-dependent recognition and excision of oxidation damage in base-excision DNA repair. Proc Natl Acad Sci U S A. 113(28):7792–7797. https://doi.org/10.1073/pnas.1604591113

Zuckerman JT et al. 2024. Functional characterization of single nucleotide polymorphic variants of DNA repair enzyme NEIL1 in South Asian populations. DNA Repair (Amst). 139:103695. https://doi.org/10.1016/j.dnarep.2024.103695

Zuckerman JT et al. 2023. Functional analyses of single nucleotide polymorphic variants of the DNA glycosylase NEIL1 in sub-Saharan African populations. DNA Repair (Amst). 129:103544. https://doi.org/10.1016/j.dnarep.2023.103544